




Functionalised iron oxide nanoparticles for multimodal optoacoustic and magnetic resonance imaging†

Gavin Bell, *^{ab} Ghayathri Balasundaram,^b Amalina Binte Ebrahim Attia, ^b
Francesca Mandino,^b Malini Olivo^b and Ivan P. Parkin *^a

The novel attachment of the optoacoustic (OA) molecules indocyanine green (ICG) and Flamma[®]774 to the core of an iron oxide (Fe₃O₄) nanoparticle has resulted in the facile synthesis of a multimodal imaging probe for both multispectral optoacoustic tomography (MSOT) imaging and magnetic resonance imaging (MRI). The nanoparticles have been analysed structurally, optically and magnetically to demonstrate the multimodal characteristics. The OA analysis of the dyes ICG and Flamma[®]774 showed that they have absorbance at the near IR wavelengths of 790 and 780 nm, respectively, when conjugated to an iron oxide core. These wavelengths are ideal for spectral unmixing of the probe intensity from any endogenous contrast, such as oxy-(HbO₂) and deoxy-hemoglobin (Hb). MRI showed that citrate capped Fe₃O₄ exhibited a good *r*₂ contrast of 230 mM⁻¹ s⁻¹, which is in line with literature values. Upon optoacoustic dye modification, the *r*₂ relaxivity coefficient is comparable with that of Flamma[®]774 iron oxide nanoparticles (FeO-774) with *r*₂ = 212 mM⁻¹ s⁻¹, showing that an OA dye attachment can have little to no effect on the MRI contrast. Indocyanine green functionalised iron oxide (FeO-ICG) nanoparticles showed an *r*₂ contrast that was dramatically reduced with *r*₂ = 5 mM⁻¹ s⁻¹. These results indicate that the facile synthesis of an effective dual modality MRI-MSOT probe can be developed using an iron oxide core and simple ligand coordination chemistry using an optoacoustic dye.

Received 31st August 2018,
Accepted 25th January 2019

DOI: 10.1039/c8tb02299b

rsc.li/materials-b

Introduction

Iron oxide nanoparticles are of great interest and have seen wide development in multiple fields and technical applications, including biomedicine, due to the manipulation of their diverse properties and high intrinsic magnetisation.¹ In particular, a low concentration of Fe₃O₄ is naturally biologically inert and has seen uses in multiple biomedical applications, from magnetic resonance imaging (MRI) and magnetic particle imaging (MPI) contrasts, drug delivery, chemical and cell separation, to magnetic hyperthermia theranostic agents,^{2–7} making magnetic nanoparticles a truly all-in-one solution for imaging and theranostic needs.

With the increased potential for exploiting magnetic properties, iron oxide nanoparticles are therefore ideal material

candidates for bio-optical probe development. Using different synthetic routes and surface modifications, nanoparticles can be tailored for very specific applications. The size and morphology can be manipulated to a preferential formation to deliver particular properties. This can be achieved through the various synthetic routes in which iron oxide can be formed. The most common in the literature are co-precipitation and hydrothermal syntheses,^{8–10} the former being used commonly as a facile mechanism for aqueous soluble nanoparticles. Hydrothermal synthesis can yield aqueous suspensions but *via* more complex surface ligand exchange chemistry.

Surface functionalisation of the particles can give improved aqueous stability, biodistribution, and add or enhance intrinsic properties.¹¹ Nanoparticles have to be stabilised in solution due to the high surface to body ratio and charged surface. This is typically achieved with neutral organic molecules and polymers, or inorganic and metallic shells,^{12–15} thus aiding the colloidal stability and reducing aggregation whilst improving the possibility for further functionalisation. Small molecule dyes have also been shown to yield a stabilisation effect on nanoparticles such as molecular near IR dyes.^{16–18} Furthermore, surface functionalisation can add targeting moieties for even greater biological affinity and impact.¹⁹ Using organic dyes to fulfill this role is of

^a Materials Chemistry Research Centre, Department of Chemistry, University College London, 20 Gordon Street, WC1H 0AJ, London, UK. E-mail: gavin.bell.14@ucl.ac.uk

^b Lab of Bio-optical Imaging, Singapore Bio-Imaging Consortium (SBIC), Agency for Science Technology and Research (A*STAR), Helios #01-02, 11 Biopolis Way, 138667, Singapore

† Electronic supplementary information (ESI) available. See DOI: 10.1039/c8tb02299b

particular interest as they have the potential to both stabilise the colloidal solution and impart novel characteristics through their absorption profile. Thus, using iron oxide based nanoparticles can lead to an attractive multimodal imaging platform with many future possibilities.

As an MRI contrast agent, iron oxide nanoparticle materials have changed the way we look inside the human body due to their infinite penetration depth and high spatial resolution and contrast of soft tissues. As a non-radiative imaging technique, high strength magnetic fields are deployed to detect the relaxation of atomic nuclei. Contrast agents are employed in MRI to facilitate the modification of the relaxation times T_1 and T_2 . Fe_3O_4 nanoparticles give strong T_2 contrasts in which the signal intensity decreases in a T_2 -weighted image. Fe_3O_4 nanoparticles can also be considered more biologically sustainable and less toxic than some commonly used gadolinium based T_1 contrast agents, which increase the signal intensity of T_1 -weighted images.²⁰ For example, literature reports show the r_1 and r_2 contrasts of various iron oxide nanoparticles, each functionalised or synthesised through various routes and resulting in different values.²¹ A conventional coprecipitation reaction coated in citrate, as explored in this manuscript, typically yields an r_2 value of $34.0 \text{ mM}^{-1} \text{ s}^{-1}$, whereas dextran coated hydrothermally synthesised iron oxide has been shown to give a value of $120 \text{ mM}^{-1} \text{ s}^{-1}$. The highest r_2 values seen in the literature are within the order of $>800 \text{ mM}^{-1} \text{ s}^{-1}$ for Zn^{2+} doped magnetic nanoparticles.²² In very recent developments, ultra-small iron oxide nanoparticles have been seen to enhance the T_1 contrast, making a Gd-free positive contrast agent, with very little chance of iron overload in the body.²³

Multispectral Optoacoustic Tomography (MSOT) is another attractive bio-imaging tool due to its ability to generate anatomical images with a deep penetration depth (3–4 cm) whilst keeping a high spatiotemporal resolution, all whilst being a non-radiative process. Typically, a short wave near-infrared (NIR) source pulses and irradiates the biological tissue and the optoacoustic probe. The NIR pulse is absorbed, which generates a small temperature spike resulting in the generation of low scattering sound waves *via* thermoelastic expansion. Ultrasound transducers detect the incoming acoustic waves that are then processed into ultrasound images. One beneficial property of an exogenous OA dye is the ability of spectral unmixing. Endogenous molecules such as oxy (HbO_2) and deoxy-hemoglobin (Hb), melanin and water all exhibit a characteristic optoacoustic spectrum.²⁴ Because of this, literature studies typically use NIR optoacoustic dyes, with absorption in the region of 700–1000 nm. Most commonly used dyes are aromatic organic structures, such as indocyanine green (ICG), methylene blue, thalocyanine, and chlorin e6.²⁵ With MSOT, it is then possible to track the dye and analyse specific cellular or molecular processes. MSOT imaging is therefore a useful tool for the imaging of tissue oxygenation and hypoxia, and blood vessel imaging for the likes of vascular disease or melanoma.²⁶

Henceforth, multimodal probe development for biological imaging is quickly becoming significant to facilitate the fast, effective and efficient gathering of the vast amounts of data

necessary for quick, decisive medical diagnoses. Combining the properties of multiple techniques gives the ability to analyse quickly and decisively by providing complementary information. Dual modality imaging techniques are common in bio-imaging, typically with MRI scanners often paired with positron emission tomography in PET-MRI scanners to provide complementary information, with the use of nanoparticle-based probes.²⁷ MRI provides intricate anatomic detail and PET offers biologically relevant functional and metabolic information at high sensitivity. With the development of new imaging probes, multimodality can be achieved, and as such, recent developments have shown the use of magnetofluorescent T_2 MRI contrast agents for targeted MR and fluorescence imaging of neural stem cells.²⁸ This interest leads to multimodal probes with a combination of MSOT and MRI. The advantage of a dual modality MSOT–MRI probe is that it can provide the combination of detailed functional and molecular information from MSOT, such as blood oxygen saturation levels, with the very high anatomical resolution given by MRI imaging.

With this desire to formulate a multimodal imaging probe based on iron oxide nanoparticles, in this manuscript, we report on the synthesis and characterisation of iron oxide nanoparticles functionalized to emit optoacoustic activity. Attachment of ICG and Flamma[®]774 dyes was achieved through activation and esterification between the magnetic particle cores and OA molecules, with the structural characteristics of the iron oxide cores largely unchanged. This initial study reveals that Flamma[®]774 OA molecule attachment can achieve a suitable contrast in both MRI and MSOT under optimum conditions.

Experimental

Materials

Indocyanine green *N*-hydroxysulfosuccinimide sodium salt (ICG sulfo-NHS) and Flamma[®]774 *N*-hydroxysulfosuccinimide sodium salt (Flamma[®]774 sulfo-NHS) were supplied by BioActs (BioActs, Korea).

Iron(III) chloride hexahydrate ($\text{FeCl}_3 \cdot 6\text{H}_2\text{O}$), iron(II) chloride tetrahydrate ($\text{FeCl}_2 \cdot 4\text{H}_2\text{O}$), ammonium hydroxide (NH_4OH), citric acid, and 2-(*N*-morpholino)ethanesulfonic acid (MES) buffer were all acquired from Sigma Aldrich.

All reagents were used as received without purification with ultra-pure double distilled water (18.2 M Ω).

Iron oxide nanoparticle synthesis

The iron oxide nanoparticles were synthesized using a coprecipitation method previously reported⁹ but with modifications. This comprises dissolving a 2 : 1 stoichiometric ratio of iron(III) : iron(II) in water and the addition of a strong base in an inert atmosphere.

In a typical reaction, iron(III) chloride, $\text{FeCl}_3 \cdot 6\text{H}_2\text{O}$ (135 mg, 50 mM), and iron(II) chloride, $\text{FeCl}_2 \cdot 4\text{H}_2\text{O}$ (50 mg, 25 mM), were added to H_2O (5 mL) degassed under the continuous flow of N_2 , forming an orange solution. The solution was heated at 70 °C for 30 minutes during which ammonium hydroxide, NH_4OH

(28%, 5 mL), was added dropwise. The solution immediately formed a black precipitate that was then heated at 70 °C for 30 minutes. Citric acid (4 mL, 0.5 g mL⁻¹) was added as a stabilising ligand and heated at 90 °C reflux for 1 hour. The black precipitate was then collected on a permanent magnet and washed with H₂O (10 mL × 3). The strong ferrofluid was dried under reduced pressure leaving a black powder.

Functionalisation of iron oxide nanoparticles for optoacoustic activity

For the attachment of optoacoustic (OA) ligands to the iron oxide nanoparticle core, a modification of a previous technique for esterification was used.

In this reaction, an NHS-activated optoacoustic derivative (ICG sulfo-NHS (10 mM) or Flamma[®] 774 sulfo-NHS (10 mM)) was added to a solution of MES buffer (pH 6.5, 50 mM, 15 mL) giving a pale green solution. Addition of the as-synthesised iron oxide nanoparticles (1 mL, before citrate stabilisation) and mixing overnight at room temperature formed the conjugated nanoparticles and a dark green solution. The nanoparticle product was collected on a permanent magnet and washed with H₂O (10 mL × 3).

Particle size and morphology

Particle size and morphology measurements were performed using a combination of transmission electron microscopy (TEM), dynamic light scattering (DLS), and UV-vis spectroscopy. TEM was performed using a JEOL JEM-2100F TEM microscope using an accelerating voltage of 120 kV. TEM samples were prepared by placing an aqueous liquid drop of the as-synthesised ferrofluid probe onto perforated carbon grids and subsequently analysing manually using Image J. DLS was performed using the aqueous ferrofluid with a Malvern Zetasizer Nano, using 1 mL of samples in a 4.5 mL plastic cuvette. The particle size was determined as a % distribution measured by intensity. Ultraviolet visible absorption spectra were obtained on a Hitachi U-2900 UV-Vis spectrophotometer from 300–1100 nm wavelength with a step size of 0.5 nm. The analyte was as-synthesised in an aqueous medium and recorded in a 1.0 mL plastic cuvette.

Animal model

All procedures performed in this study involving animals were in accordance with ethical standards and approved by the Institutional Animal Care and Use Committee, A*STAR Biological Resource Centre, Singapore (IACUC #151085/140898). The animals used were NCr nude mice (U87 mg xenograft) from InVivos (Singapore). 8–10 weeks old NCr nude female mice weighing between 20–25 g were used for this study. 200 µL of 5 × 10⁶ U87MG cells (ATCC) was mixed with matrigel in 1:1 volume and inoculated on the right flank of the mouse, and imaging procedures were performed 3 weeks later.

Multispectral optoacoustic tomography

Multispectral optoacoustic tomography was performed using an iThera Medical MSOT inVision 512-echo small animal imaging system.²⁹ Phantom samples were 180 µL and prepared

in a 10 cm cylindrical polyurethane phantom fabricated to simulate the characteristics and optical properties of mice and submerged in a water bath to aid with acoustic detection. The optoacoustic detection wavelength was in the range of 680–980 nm at 5 nm intervals across a length of 5 mm of the phantom at 0.5 mm slices.

Briefly, a tuneable optical parametric oscillator (OPO) pumped by a Nd:YAG laser provides excitation pulses with a duration of 9 ns at a repetition rate of 10 Hz with a wavelength tuning speed of 10 ms and a peak pulse energy of 100 mJ at 730 nm. Ten arms of a fibre bundle provide even illumination of a ring-shaped light strip of approx. 8 mm width. OA signals were acquired using a 512-element concave transducer array spanning a circular arc of 270°. During MSOT measurements, the phantom is translated through the transducer array along its axis to acquire the transverse image slice set.

For *in vivo* imaging, FeO-774 (100 mM w/Fe in 5 µL saline) was administered through an intratumoral injection. Ultrasound gel was applied on the mouse skin surface and measurements were recorded in water at 34 °C for good acoustic coupling. An animal holder with a thin polyethylene membrane was used to prevent direct contact between the mouse and the water. A volumetric region of interest (ROI) consisted of multiple transverse slices with an inter-slice distance of 0.5 mm. Ten frames were acquired and averaged for each wavelength (680, 700, 760, 770, 780 (the FeO-774 absorption peak), 790, 800 (the isosbestic point of Hb and HbO₂), 850, 900 nm). MSOT imaging was performed pre-injection, and 15 minutes post-injection. For all concentrations used, Fe₃O₄ was freeze dried, weighed, and re-dispersed in aqueous solvent.

Image reconstruction and processing

MSOT images were reconstructed using a model-linear algorithm using the ViewMSOT proprietary software. Thereafter, spectral unmixing was performed to resolve individual components from different chromophores in the system. For each pixel in the image, the method fits the total measured optoacoustic spectrum to the known absorption spectra of the individual chromophores, based on least-squares linear regression.

Magnetic resonance imaging

MRI relaxivity of the nanoparticles was evaluated by using a 7 Tesla Bruker Clinscan MRI system. *T*₂-weighted relaxation times were determined using a multiecho spin-echo sequence (repetition time (TR): 4000 ms; TE: 17.9–250.6 ms). *r*₂ relaxivities were obtained from the slope of 1/*T*₂ versus molar [Fe] concentration plots. Phantoms were prepared in 500 µL samples using a 1 mL plastic syringe, placed inside the coil.

Animals were anaesthetised using isoflurane. Briefly, anaesthesia was induced with 4% isoflurane; animals were then positioned on an MRI-compatible cradle. Isoflurane was lowered to 1.5% for the whole MRI-scanning session.

Animal temperature was maintained at 37 °C. Data were acquired on an 11.75 T Biospec (Bruker BioSpin MRI, Ettlingen, Germany) equipped with a BGA-S gradient system, a linear

volume resonator coil for transmission and a 10 mm multi-purpose surface receiver coil positioned over the tumour.

Images were acquired using Paravision 6.0.1 software. Gradient-Echo MRI images were acquired using a fast low angle shot (FLASH) sequence: field of view (FOV) = $20 \times 20 \text{ mm}^2$, number of slices = 20, slice thickness = 0.4, slice gap = 0.3 mm, MD = 192×192 , TR = 15 ms, TE = 3 ms, flip angle = 50° , volumes = 1, and bandwidth = 250 kHz. Two FLASH images were acquired: one before the contrast agent injection, as a baseline, and one 5' after the injection.

Results and discussion

Synthesis

All iron oxide nanoparticles were synthesised using the coprecipitation method, in which iron(II) and iron(III) salts were dissolved aqueously, heated and reduced with a strong ammonium hydroxide base. The citrate stabilised nanoparticles are hereon referred to as FeO-C. Further functionalisation of the particles was achieved through the novel covalent attachment of the optoacoustic dyes to the surface of the iron oxide particle using sulfo-NHS activated dyes. The activation of the dye allows facile attachment of the molecule to the Fe-OH surface of the iron oxide nanoparticles (Fig. 1) *via* a common NHS esterification mechanism.³⁰ Upon successful covalent binding, it was noted that the supernatant was colourless when the magnetic particles were collected using a permanent magnet. To verify this, we not only monitored the absorption of the dye onto the particle surface, but also when the dye was added without an activated moiety, the dye remained in solution and gave a green supernatant when the particles were collected. These dyes include indocyanine green and Flamma[®]774. These particles are, therefore, referred to as FeO-ICG and FeO-774 respectively. The final products were all dispersible in water and formed strong magnetic ferrofluids.

Structural characterisation of optoacoustic iron oxide nanostructures

Electron microscopy shows the single core size and structure of the nanoparticle formations before and after dye conjugation.

As can be seen in the TEM images and corresponding histograms (Fig. 2) (of 147 particles), the citrate capped nanoparticles, FeO-C, are of a spherical shape with a mean core diameter of $9 \pm 3 \text{ nm}$ with some polydispersity. The microscopy also shows that the synthesis of an FeO-OA dye nanoparticle has little effect on the morphological behavior of the particles.

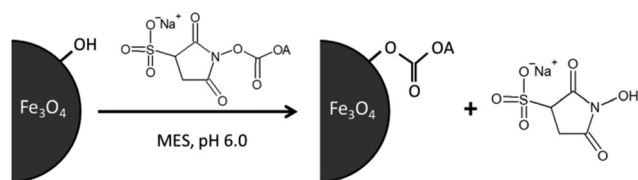


Fig. 1 Reaction scheme of the optoacoustic molecule (OA) attachment to the Fe_3O_4 surface, where OA represents ICG or Flamma[®]774.

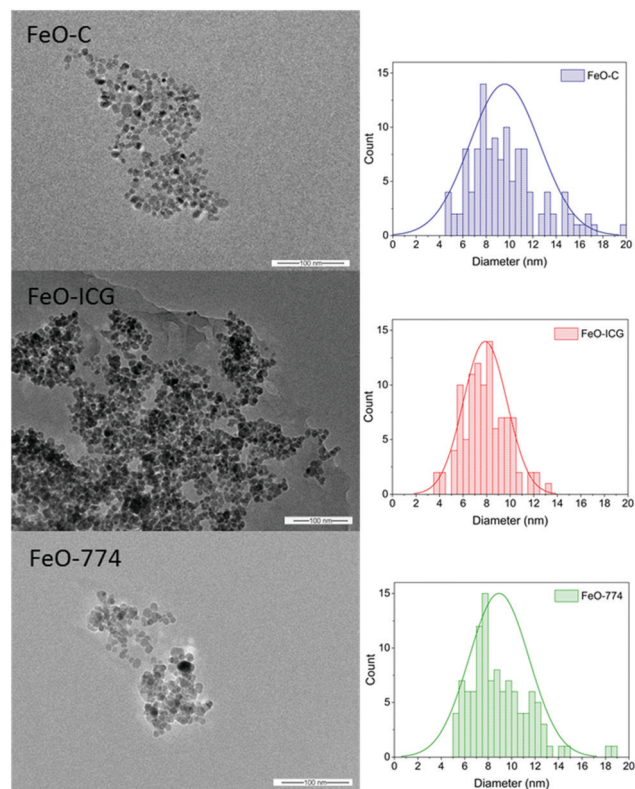


Fig. 2 TEM images of citrate capped iron oxide nanoparticles, FeO-C, and optoacoustic capped iron oxide nanoparticles, FeO-ICG and FeO-774. Included are the respective histograms for the diameter of the particles, showing the similar sizes of the functionalised nanoparticles, spherical morphology and aggregation.

ICG capped nanoparticles have a mean diameter of $8 \pm 2 \text{ nm}$, (of 156 particles) whilst Flamma[®]774 capped Fe_3O_4 has a mean diameter of $9 \pm 3 \text{ nm}$ (of 162 particles), as shown by the histograms and in Table 1. This is common and comparable with previously synthesized nanoparticles formed using coprecipitation methods.⁹

However, the TEM images show that there is aggregation of the nanoparticles when stabilised with both citrate and the OA dyes. This was confirmed *via* dynamic light scattering (DLS) showing *in situ* agglomeration with a Z-average hydrodynamic diameter, ϕ_H , of 110 nm and a polydispersity index (PDI) of 0.24 for FeO-C (Table 1). DLS also showed that the OA dyes were less effective stabilizing ligands than the commonly used citrate capping agent. ϕ_H is on the order of 310 nm and 150 nm for FeO-ICG and FeO-774, respectively, with ICG being the least effective stabilising ligand and showing the most polydispersity of the particles, with a PDI of 0.36.

Table 1 Crystallite size and particle surface charge of the iron oxide and iron oxide-optoacoustic nanoparticles determined *via* TEM and DLS characterisation

Sample	TEM/nm	DLS/nm	PDI	Zeta potential/mV
FeO-C	9 ± 3	110	0.235	-21.4
FeO-774	8 ± 2	150	0.239	-24.0
FeO-ICG	9 ± 3	310	0.363	-16.9

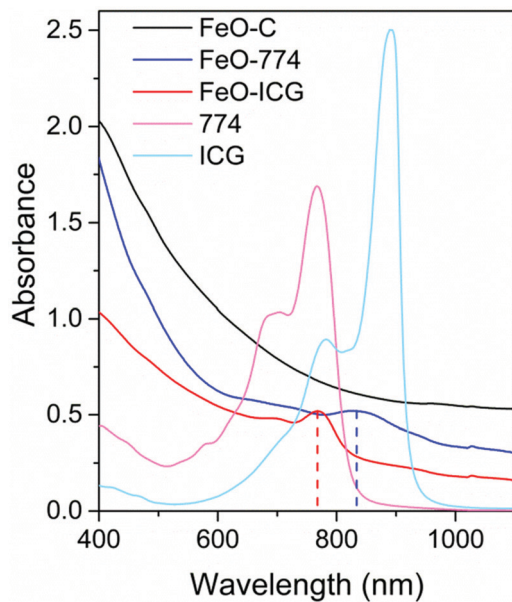


Fig. 3 UV visible absorption spectrum of FeO-C, FeO-ICG and FeO-774. NIR absorption of the particles is shown at 780 nm for FeO-ICG and at 830 nm for FeO-774, with no NIR peak for FeO-C. The spectra also include the reference spectra of the dyes, ICG and Flamma[®]774.

The clustering of the nanomaterials is random in nature and has no defined orientation.³¹ This limits the usability of these particles as the high hydrodynamic radius can lead to incompatibility with biological barriers. Furthermore, the particles can often drop from the suspension as the aggregates grow large meaning reproducibility can be troublesome.

The main driving force in aggregation is the charged nature of the surface of the individual particles. All synthesized samples hold a negative zeta potential. FeO-ICG has the weakest negative charge at -16.9 mV, which leads to the greater aggregation seen.

Verification for the attachment of the OA dye onto the surface of the iron oxide nanoparticles can be seen in the UV-vis absorption spectra in Fig. 3. After thorough extraction of the iron oxide cores through magnetic extraction and washing with H₂O, the absorption peaks for ICG and Flamma[®]774 are both visible at 830 nm and 780 nm, respectively. This is in accordance with the standard absorbance of unbound free ICG, at 800 nm, and Flamma[®]774, at 774 nm. This shows a blueshift in the absorption of the dyes, which could be attributed to the molecule being bound to the metallic particle core.³²

Multispectral optoacoustic tomography

The attachment of an optoacoustic chromophore to the surface of the iron oxide nanoparticles allowed us to perform optoacoustic tomography to achieve a multimodal probe. The optoacoustic spectra and the subsequent images were all obtained using a polyurethane phantom model. The optoacoustic spectra (Fig. 4) were plotted in contrast with the endogenous contrast agents oxy (HbO₂) and deoxy-hemoglobin (Hb). For an exogenous contrast agent to be visible, the optoacoustic spectra must not include interference from any of the internal biological contrasts.

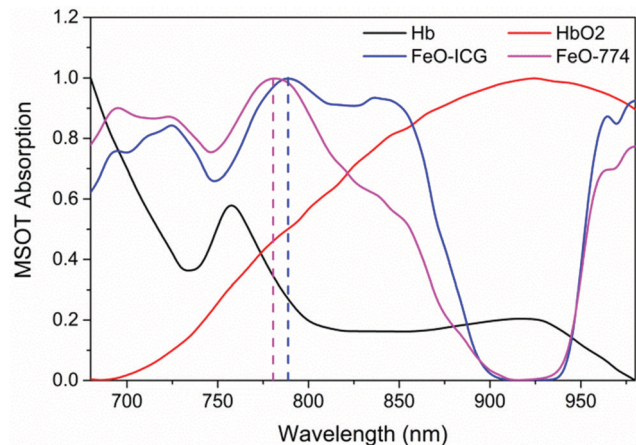


Fig. 4 Optoacoustic absorption spectra of FeO-ICG and FeO-774, at 100 mM each, along with the contrast with the endogenous contrast agents oxy (HbO₂) and deoxy-hemoglobin (Hb). The normalised MSOT absorption peaks at 780 nm for FeO-774 and 790 nm for FeO-ICG. Variation in the peak wavelength absorbance makes spectral un-mixing possible.

The optoacoustic spectra (Fig. 4) show the MSOT absorption spectra for Fe-ICG and FeO-774, which are represented by peaks of 790 and 780 nm, respectively. These wavelengths fall between the 755 nm peak of Hb and the rising absorbance of HbO₂, thus making spectral unmixing of the probe possible against these endogenous contrasts.

In contrast, the optoacoustic spectra of FeO-C (see appendix) have low intensity in this window and are not sufficient to un-mix the signals of the HbO₂ spectra. Therefore, with the conjugation of the OA dyes, ICG or Flamma[®]774, however, the optoacoustic signal has been amplified, making spectral un-mixing possible.

Multi-spectral processing of the optoacoustic absorption spectra over concentration shows the average MSOT signal acquired from the FeO-OA particles. The trend, shown in Fig. 5, shows the signal obtained at increasing concentration. As concentration increases, so too does the MSOT signal, reaching saturation at ~ 100 mM [Fe₃O₄]. The signal for both FeO-ICG and FeO-774 shows comparable intensity and the linear fit of the concentration curve shows similar absorption profiles. This demonstrates that FeO-ICG and FeO-774 are both effective and suitable MSOT probes, even at low concentrations < 100 mM [Fe₃O₄]. However, the gradient of the linear fit is greater for the absorption of FeO-774. Fig. 5 shows a steeper gradient of 0.032 for FeO-774 compared to 0.025 for FeO-ICG, thus allowing us to show that FeO-774 is the better MSOT probe with a higher OA efficiency. Full saturation plots can be found in the appendix.

Magnetic resonance imaging

For a complete multimodal probe, the nanoparticles must also exhibit a contrast for MRI. For this, a concentration gradient in a phantom study was achieved in a 7 Tesla Bruker Clinscan MRI system. This shows the level of T_2 relaxation caused by the iron oxide core from the equation:

$$M_{xy}(t) = M_{xy}(0)e^{-t/T_2}$$

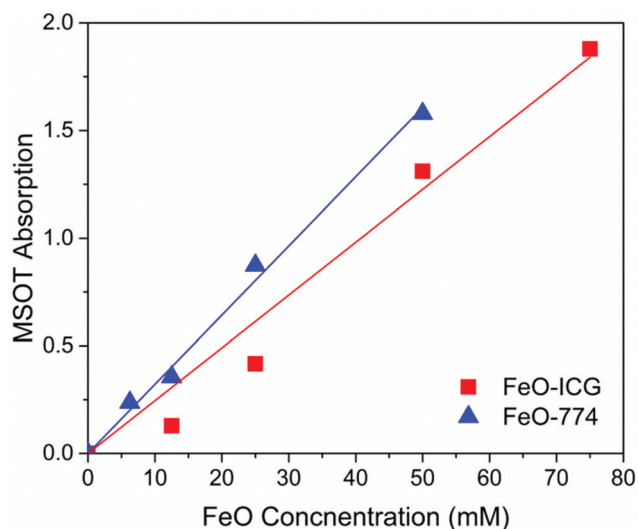


Fig. 5 Concentration gradient with respect to MSOT intensity and linear fit for the MRI-MSOT probe nanoparticles FeO-ICG and FeO-774.

where $M_{xy}(t)$ is the nuclear spin magnetization vector and t is the time. This is easily extracted from an exponential fit of the relaxation curves.

The scan was performed over increasing scan lengths from t_1 , 17.9 ms, to t_{14} , 250.6 ms. Furthermore, the spin relaxivity $R^2 = 1/T_2$, which shows the degree of the T_2 -weighted contrast of the MRI image, and a linear plot of R^2 vs. $[Fe]$ (the concentration of the magnetic atoms) give the relaxivity coefficient, r_2 , via the gradient.³³

We can see from the gradient of the plots in Fig. 6 that the spin echo relaxivity, r_2 , is shown to be $230 \text{ mM}^{-1} \text{ s}^{-1}$ for FeO-C, $212 \text{ mM}^{-1} \text{ s}^{-1}$ for FeO-774 and only $5.2 \text{ mM}^{-1} \text{ s}^{-1}$ for FeO-ICG. There has been little effect of the addition of Flamma[®]774 on the relaxivity of the nanoparticles. Whereas, ICG has shown a large decrease in R^2 , showing nearly negligible contrast in MRI, and a poor linear fit ($R^2 = 0.006$). Even at higher concentrations of FeO-ICG, there is still no definitive MRI r_2 relaxivity coefficient seen. This can be compared with the r_2 values of an industry standard and commercial iron oxide T_2 contrast agent, Resovist, which has an r_2 relaxivity of $151 \text{ mM}^{-1} \text{ s}^{-1}$.⁵

One probable cause for this discrepancy with FeO-ICG is thought to be due to the stabilisation and dispersion of the magnetic nanoparticle cores.³⁴ As stated previously (Table 1), FeO-ICG has a hydrodynamic radius of 311 nm, which is up to a three-fold increase in hydrodynamic diameter. FeO-C and FeO-774 are shown to have ϕ_H values of 108 nm and 146 nm, respectively.

For comparison, the hydrodynamic radius of Resovist is reported to be 45–60 nm.⁵ This is a factor of two smaller than that of the FeO-C and FeO-774 nanoparticles and a factor of 4 smaller than Fe-ICG. Furthermore, indocyanine green is not a large stabilising molecule or a high molecular weight organic polymer. Therefore, the resultant ϕ_H is due to the aggregation of the negatively charged Fe_3O_4 cores and not the ligand dispersion around the core. The TEM images (Fig. 2) also show that the aggregation of the FeO-ICG nanoparticles is greater.

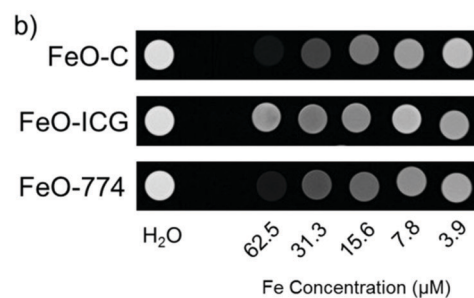
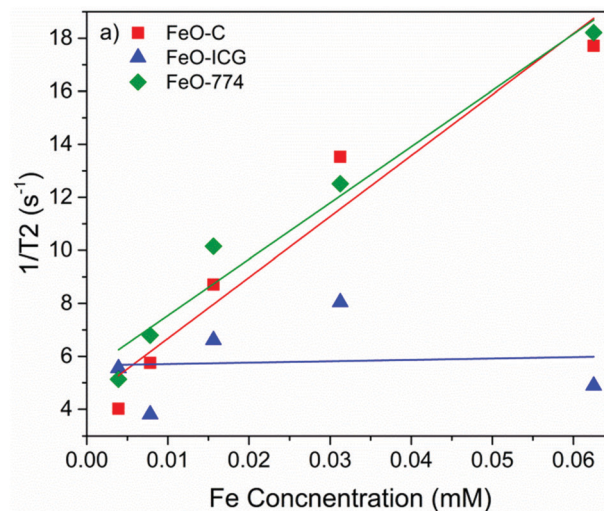


Fig. 6 (a) Plot of $1/T_2$ against $[Fe]$ concentration and (b) visual representation of the concentration dependent T_2 -weighted MRI contrast for FeO-C, FeO-774, and FeO-ICG. The positive linear trend gives the R^2 reflexivity values for the nanoparticle materials. Included is the background of H_2O to show the intensity of the contrast.

The images show much larger clusters of particles compared to those of FeO-C and FeO-774.

This shows that aggregation of the particles can play a large role in the contrast of MRI agents. Well dispersed particles like those coated in citrate or the polymer based iron oxide particles in the literature have a high contrast and relaxivity coefficient. Therefore, development of the stabilisation and encapsulation of the optoacoustically active iron oxide through organic and bio-polymer chemistry is currently being investigated.

In vivo imaging

To determine if the multimodality of the FeO-OA nanoparticles is translatable to animal models and real world biological systems, *in vivo* analysis was performed. This was achieved using the mouse model. Nanoparticle delivery was achieved with an intratumoral injection of the nanoparticle sample at 100 mM Fe_3O_4 concentration in a saline solution and scanning 15 minutes post injection. FeO-774 nanoparticles were analysed *in vivo* as FeO-774 provided both the highest optoacoustic signal output and the greatest MRI T_2 contrast when compared to the FeO-ICG nanoparticles. Due to the disparity between the relatively low concentration of Flamma[®]774 on the surface of the nanoparticles compared to the iron oxide in the core,

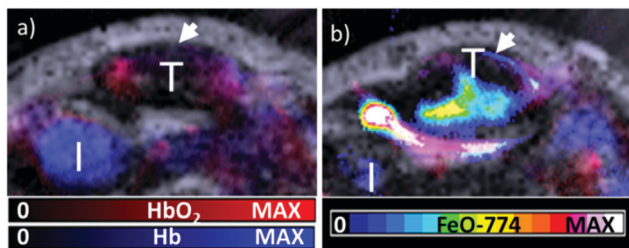


Fig. 7 (a) Oxy- and deoxyhemoglobin maps overlaid on ultrasound images of the U87MG tumor (T indicated by white arrows) implanted subcutaneously in the Ncr nude mouse obtained before contrast agent administration and (b) the 15 minute post-injection scan after FeO-774 intra-tumour injection showing the high optoacoustic signal localisation of the FeO-774 nanoparticles in the tumour.

the MRI was a much more sensitive imaging technique. This means that the concentration of nanoparticles needed for MSOT was far higher than that for MRI. For this, a 100 mM aqueous solution of FeO-774 was injected once for both scans of MSOT and MRI producing high signal and high contrast images.

MSOT images are shown in Fig. 7 and show the pre-scan where there is some negligible background signal from the FeO-774 wavelength. This is expected as the FeO-774 spectra (see Fig. 4) have multiple minor peaks that do partially overlap with the endogenous contrast agents Hb and HbO₂. Upon intratumoral injection, spectral unmixing of the MSOT signal isolated the exogenous FeO-774 optical contrast agent from the endogenous spectra. It can be seen that the signal intensity of the spectrally unmixed MSOT spectra is greatly increased at the tumour site on the right flank of the mouse due to the increased presence of FeO-774 nanoparticles. The retention time for the nanoparticles in the tumour is high due to the method of introduction of the contrast agent.

Following the MSOT scan (Fig. 7), the mouse model was transferred, without further injection, to acquire MRI images (Fig. 8) and they showed that the addition of FeO-774 nanoparticles leads to a strong t_2 contrast with the pre-scan tumour (white region) becoming negatively contrasted upon addition of FeO-774 nanoparticles. This is expected due to the well known nature of Fe₃O₄ nanoparticles being a strong t_2 contrast agent, and this demonstrates that the nanoparticles are still stable in the mouse model and do not aggregate and lose MRI contrast

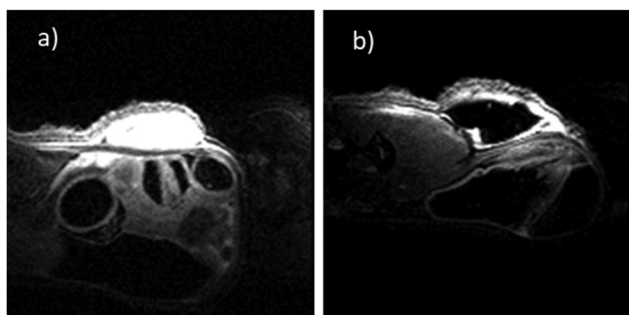


Fig. 8 MRI images for (a) pre-scan and (b) 15 min post injection showing the increase in t_2 contrast within the tumour in the presence of FeO-774 nanoparticles.

properties. Further, this shows that FeO-774 nanoparticles are multimodal in nature and work as desired in both MRI and MSOT spectroscopy.

Conclusions

In conclusion, we have shown a facile way to make a multimodal MRI-MSOT nanoparticle probe using a novel surface attachment chemistry of an OA dye onto the surface of iron oxide nanoparticles. The nanoparticles that we report show an enhanced optoacoustic signal due to the presence of the OA dye, ICG or Flamma[®]774, with FeO-774 showing the highest MSOT efficiency. The obtained optoacoustic spectra exhibit a clear peak in the near-IR wavelength region of 790 and 780 nm for FeO-ICG and FeO-774, respectively. This makes spectral unmixing of FeO-OA nanoparticles and the endogenous contrast Hb and HbO₂ possible.

Furthermore, we have demonstrated that FeO-774 displays a good MRI r_2 contrast of 212 mM⁻¹ s⁻¹, which is similar to the citrate coated FeO-C r_2 relaxivity coefficient of 230 mM⁻¹ s⁻¹. This shows that OA dye functionalisation has little to no effect on the MRI properties of iron oxide nanoparticles. However, FeO-ICG does show a vastly reduced contrast, at 5 mM⁻¹ s⁻¹. This can be attributed to the surface stabilisation produced using ICG molecules. TEM and DLS analysis showed much greater aggregation and clustering compared to iron oxide nanoparticles coated with citrate or Flamma[®]774 conjugation.

In vivo analysis also demonstrated how the nanoparticles can be used for spectral unmixing of the nanoparticle absorption wavelengths and the endogenous contrast agents using MSOT. Furthermore, the nanoparticles showed high MRI contrast due to the good hydrodynamic dispersity and stability of the iron oxide cores. This also showed that FeO-774 nanoparticles are stable in biological systems and the MRI or MSOT signals were not quenched.

From this, we have determined that FeO-774 is the best iron oxide core based MSOT-MRI probe that we have developed using a facile and simple chemical synthesis. However, further refinement of the nanoparticle structures is still necessary, with stabilization and aggregation being key areas of development in the progression to make an ideal MSOT-MRI optoacoustic probe. Development of a specific targeting probe is of high interest and impact for clinical studies where an intravenous administration of the contrast is more desirable using the functionality of attached enzymes and proteins. This still needs further research and refinement of current iron oxide cores to achieve greater monodispersity, size and biological stability.

Conflicts of interest

There are no conflicts to declare.

Acknowledgements

We would like to acknowledge and thank the EPSRC Eng. D. (Award Ref: 1572230) and A*STAR for funding towards the

studentship of G. Bell. We would also like to thank Michael Ng for assistance in MRI data collection at SBIC A*STAR.

References

- 1 B. Hamm, T. Staks, M. Taupitz, R. Maibauer, A. Speidel, A. Huppertz, T. Frenzel, R. Lawaczeck, K. J. Wolf and L. Lange, *J. Magn. Reson. Imaging*, 1994, **4**, 659–668.
- 2 Q. A. Pankhurst, J. Connolly, S. K. Jones and J. Dobson, *J. Phys. D: Appl. Phys.*, 2003, **167**, R167–R181.
- 3 Q. A. Pankhurst, N. Thanh, S. Jones and J. Dobson, *J. Phys. D: Appl. Phys.*, 2009, 224001.
- 4 L. Thomas, L. Dekker, M. Kallumadil, P. Southern, M. Wilson, S. Nair, Q. Pankhurst and I. Parkin, *J. Mater. Chem.*, 2009, **19**, 6529–6535.
- 5 Y.-X. J. Wang, *Quant. Imaging Med. Surg.*, 2011, **1**, 35–40.
- 6 R. M. Ferguson, A. P. Khandhar, S. J. Kemp, H. Arami, E. U. Saritas, L. R. Croft, J. Konkle, P. W. Goodwill, A. Halkola, J. Rahmer, J. Borgert, S. M. Conolly and K. M. Krishnan, *IEEE Trans. Med. Imaging*, 2015, **34**, 1077–1084.
- 7 B. Chertok, B. A. Moffat, A. E. David, F. Yu, C. Bergemann, B. D. Ross and V. C. Yang, *Biomaterials*, 2008, **29**, 487–496.
- 8 S. Laurent, D. Forge, M. Port, A. Roch, C. Robic, L. V. Elst and R. N. Muller, *Chem. Rev.*, 2008, **108**, 2064–2110.
- 9 G. Bell, L. K. Bogart, P. Southern, M. Olivo, Q. A. Pankhurst and I. P. Parkin, *Eur. J. Inorg. Chem.*, 2017, 2386–2395.
- 10 S. Ge, X. Shi, K. Sun, C. Li, C. Uher, J. R. Baker, M. M. B. Holl and B. G. Orr, *J. Phys. Chem. C*, 2009, **113**, 13593–13599.
- 11 W. Wu, Q. He and C. Jiang, *Nanoscale Res. Lett.*, 2008, **3**, 397–415.
- 12 I. Robinson, L. D. Tung, S. Maenosono, C. Wälti and N. T. K. Thanh, *Nanoscale*, 2010, **2**, 2624–2630.
- 13 M. Lattuada and T. A. Hatton, *Langmuir*, 2007, **23**, 2158–2168.
- 14 H. L. Ding, Y. X. Zhang, S. Wang, J. M. Xu, S. C. Xu and G. H. Li, *Chem. Mater.*, 2012, **24**, 4572–4580.
- 15 R. Alwi, S. Telenkov, A. Mandelis, T. Leshuk, F. Gu, S. Oladepo and K. Michaelian, *Biomed. Opt. Express*, 2012, **3**, 2500–2509.
- 16 Q. Tang, Y. An, D. Liu, P. Liu and D. Zhang, *PLoS One*, 2014, **9**, 1–8.
- 17 S. Luo, E. Zhang, Y. Su, T. Cheng and C. Shi, *Biomaterials*, 2011, **32**, 7127–7138.
- 18 S. Lee, R. G. Thomas, M. J. Moon, H. J. Park, I. K. Park, B. I. Lee and Y. Y. Jeong, *Sci. Rep.*, 2017, **7**, 1–14.
- 19 B. Stella, S. Arpicco, M. T. Peracchia, D. Desmaele, J. Hoebeke, M. Renoir, J. D'Angelo, L. Cattel and P. Couvreur, *J. Pharm. Sci.*, 2000, **89**, 1432–1442.
- 20 M. Rogosnitzky and S. Branch, *Biomaterials*, 2016, **29**, 365–376.
- 21 N. Lee, D. Yoo, D. Ling, M. H. Cho, T. Hyeon and J. Cheon, *Chem. Rev.*, 2015, **115**, 10637–10689.
- 22 J. Jang, H. Nah, J. Lee, S. H. Moon, M. G. Kim and J. Cheon, *Angew. Chem., Int. Ed.*, 2009, **4**, 1234–1238.
- 23 H. Wei, O. T. Bruns, M. G. Kaul, E. C. Hansen, M. Barch, A. Wiśniowska, O. Chen, Y. Chen, N. Li and S. Okada, *et al.*, *Proc. Natl. Acad. Sci. U. S. A.*, 2017, **114**, 2325–2330.
- 24 A. Roggan, M. Friebel, K. Dorschel, A. Hahn and G. Muller, *J. Biomed. Opt.*, 1999, **4**, 36–46.
- 25 C. J. H. Ho, G. Balasundaram, W. Driessen, R. McLaren, C. L. Wong, U. S. Dinish, A. B. E. Attia, V. Ntziachristos and M. Olivo, *Sci. Rep.*, 2014, **4**, 5342.
- 26 A. B. E. Attia, S. Y. Chuah, D. Razansky, C. J. H. Ho, P. Malempati, U. S. Dinish, R. Bi, C. Y. Fu, S. J. Ford, J. S. S. Lee, M. W. P. Tan, M. Olivo and S. T. G. Thng, *Photoacoustics*, 2017, **7**, 20–26.
- 27 J. Garcia, T. Tang and A. Y. Louie, *Nanomedicine*, 2015, **10**, 1343–1359.
- 28 Y.-K. Peng, C. N. P. Lui, T.-H. Lin, C. Chang, P.-T. Chou, K. K. L. Yung and S. C. E. Tsang, *Faraday Discuss.*, 2014, **175**, 13–26.
- 29 S. Morscher, W. H. P. Driessen, J. Claussen and N. C. Burton, *Biochem. Pharmacol.*, 2014, **2**, 103–110.
- 30 D. Bartczak and A. G. Kanaras, *Langmuir*, 2011, **27**, 10119–10123.
- 31 E. M. Hotze, T. Phenrat and G. V. Lowry, *J. Environ. Qual.*, 2010, **39**, 1909.
- 32 C. Niu, Y. Xu, S. An, M. Zhang, Y. Hu, L. Wang and Q. Peng, *Sci. Rep.*, 2017, **7**, 1–10.
- 33 S. H. Koenig and K. E. Kellar, *Magn. Reson. Med.*, 1995, **34**, 227–233.
- 34 U. I. Tromsdorf, N. C. Bigall, M. G. Kaul, O. T. Bruns, M. S. Nikolic, B. Mollwitz, R. A. Sperling, R. Reimer, H. Hohenberg, W. J. Parak, S. Forster, U. Beisiegel, G. Adam and H. Weller, *Nano Lett.*, 2007, **7**, 2422–2427.